Birefringence properties of the human cornea measured with polarization sensitive optical coherence tomography

HITZENBERGER C.K., GÖTZINGER E., PIRCHER M. [1]

ABSTRACT

We map the three-dimensional distribution of birefringence of the normal human cornea and provide insight into structures and mechanisms causing corneal birefringence, establishing standard patterns of 3D birefringence distribution.

A polarization sensitive optical coherence tomography (PS-OCT) system was developed that allows measurement and imaging of three tissue parameters simultaneously: reflectivity, retardation, and slow optic axis orientation. This instrument was used to obtain 3D PS-OCT data sets of normal human corneas in vitro. From the 3D data sets, conventional cross sectional, as well as en face images of reflectivity, retardation, and optic axis orientation were derived. Preliminary results from a healthy cornea in vivo and a keratoconus cornea in vitro are also presented.

In transversal direction the retardation distribution of the normal cornea has a radially symmetric shape; retardation is lowest at the center of the cornea and increases towards the periphery. At peripheral regions, retardation also increases with depth. The distribution of the optic axis is not constant with the parallel illumination scheme used. Optic axis orientation is an approximately linear function of azimuth angle, however, if averaged over the entire cornea, a preferential optic axis orientation is observed. In a keratoconus cornea, the normal birefringence pattern is heavily distorted.

The results provide additional insight into corneal birefringence as compared to published work where corneal birefringence is usually averaged over a larger area. The results can be explained by a birefringence model based on stacked collagen fibril lamellae of different orientations. The observed birefringence patterns in normal corneas might be used as standard patterns for comparisons with pathologic changes.

KEYWORDS

Cornea, polarization, optical coherence tomography

RÉSUMÉ

Nous cartographions la répartition tridimensionnelle de biréfringence de la cornée humaine normale et fournirons un aperçu des structures et des mécanismes provoquant la biréfringence cornéenne pour établir des modèles standard de la répartition de biréfringence en 3D. Un système de tomographie par cohérence optique sensible à la polarisation (TCO-SP) a été développé, lequel permet la mesure et l'imagerie simultanées de trois paramètres tissulaires : réflectivité, retard, et orientation de l'axe optique lent. Cet instrument a été utilisé pour obtenir des ensembles de données 3D par TCO-SP de cornées humaines normales *in vitro*. Des images transversales conventionnelles ainsi que des images de face de réflectivité, de retard et d'orientation de l'axe optique ont été dérivés des ensembles de données 3D. Des résultats préliminaires issus d'une cornée saine *in vivo* et d'une cornée kératocône *in vitro* sont aussi présentés. Dans une direction transversale, la répartition du retard de la cornée normale présente une forme radialement symétrique;

.....

[1] *Center for Biomedical Engineering and Physics, Medical University of Vienna, Austria*

le retard le plus faible se situe au centre de la cornée et augmente vers la périphérie. Au niveau des régions périphériques, le retard augmente aussi avec la profondeur. La répartition de l'axe optique n'est pas constante avec le schéma d'éclairage parallèle utilisé. L'orientation de l'axe optique est une fonction pratiquement linéaire de l'angle d'azimut, cependant, si elle est moyennée sur la totalité de la cornée, une orientation préférentielle de l'axe optique est observée. Dans une cornée kératocônique, le modèle normal de biréfringence est fortement distordu. Les résultats fournissent un aperçu supplémentaire de la biréfringence cornéenne par rapport au travail publié dans lequel la biréfringence cornéenne est habituellement moyennée sur une plus grande surface. Les résultats peuvent s'expliquer par un modèle de biréfringence basé sur des lamelles de fibrilles de collagène empilées dans différentes orientations. Les modèles de biréfringence observés dans des cornées normales peuvent être utilisées comme des modèles standard pour effectuer des comparaisons avec les changements pathologiques.

MOTS-CLÉS

Cornée, polarisation, tomographie par cohérence optique

INTRODUCTION

It has long been known that the cornea is optically birefringent and several papers on corneal birefringence have been published. An overview of the work on corneal birefringence can be found in Bour L.J.[3] Different models on the nature of corneal birefringence have been reported which are partly contradictory: e.g. the cornea was modeled as a uniaxial [30] and a biaxial crystal.[31] The present state of knowledge on corneal structure and its relation to birefringence can be summarized as follows: the corneal tissue is arranged in several layers. Over 90 % of its thickness is made up by the stroma, which consists of approximately 200 lamellae with a thickness of 1.5-2.5 μm. Each of these lamellae is composed of parallel collagen fibrils embedded in an optically homogeneous ground substance.[9,24] For modeling the birefringence of the cornea, each lamella is regarded as a birefringent plate with its slow axis lying along the direction of the collagen fibrils.[11] The fibrils in successive lamellae are usually oriented at large, approximately orthogonal angles to each other, so that the birefringence properties of successive lamellae cancel each other largely. X-ray studies of the cornea have revealed two preferred directions of orientation in the cornea. 60 % of the fibrils are oriented within the 45° sectors around the inferior-superior and nasal-temporal preferred directions, while 40 % are oriented in the oblique sectors in between.[6,25] A slight prevalence of one lamella orientation causes a net retardation and a net optic axis orientation.

The importance of a detailed knowledge on the corneal birefringence lies mainly in the fact that several techniques of ophthalmic imaging use polarized light in one or another way. Scanning laser polarimetry [10] is especially noteworthy in this context. This technique, which is used for glaucoma diagnostics, measures and images the distribution of retinal nerve fiber layer birefringence through the cornea. Reliable results therefore require a precise knowledge of corneal retardation and slow axis orientation.[33] While initially a fixed retardation and axis orientation was assumed for the entire population, a comprehensive study has shown that these parameters vary considerably between individual subjects.[23]

The majority of studies on corneal birefringence performed measurements only in the central cornea. However, some studies also reported on the distribution of birefringence in the cornea.[4-5,20,31] The results of these studies are somewhat contradictory: While Van Blockland and Verhelst report a saddleback distribution of corneal birefringence,[31] Bour and Lopez Cardozo,[4] and Bueno and Vargas-Martin[5] observed an increase of retardation with distance from the corneal apex in all radial directions. Results on slow axis distribution were also contradictory.[5, 20]

In this paper, we report results on the birefringence of the human cornea obtained with a rather new imaging technique: polarization sensitive optical coherence tomography (PS-OCT).[8] This independent method has been shown to be able to shed more light on the somewhat contradictory results of previous studies.[14] We present the method and subsequently use it to obtain 3D data sets of the distribution of retardation and (cumulative) slow axis in human cornea in vitro. From these data sets we derive cross sectional PS-OCT images and en face OCT images demonstrating the distribution of retardation and slow axis orientation at the posterior corneal surface. The results are discussed and explained by a birefringence model based on stromal lamella stacks. Finally, we show first results obtained in pathologic corneas in vitro and in healthy corneas in vivo and discuss the differences and possible implications for corneal diagnostics.

METHODS

Description of instrument

Optical coherence tomography is a non-invasive imaging technique that generates high resolution cross sectional images of biological tissue.[2,12,18] Based on low coherence interferometry, the technique measures spatially resolved backscattered intensity in transparent and scattering

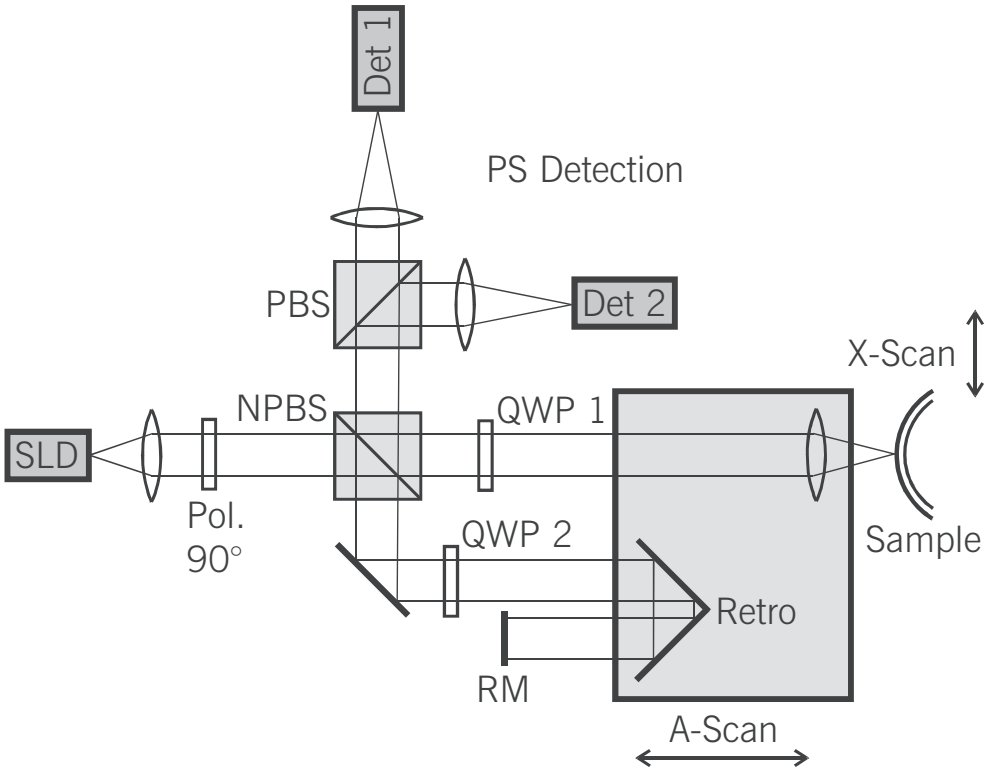

Fig. 1. Sketch of PS-OCT instrument. Det, detectors; NPBS, non-polarizing beam splitter; PBS, polarizing beam splitter; Pol., polarizer; PS detection, polarization sensitive detection; QWP, quarter wave plate; Retro, retro-reflector; RM, reference mirror; SLD, super luminescent diode.

samples. PS-OCT takes advantage of the additional polarization information carried by the reflected light and can provide quantitative information on tissue birefringence.[8] While early work on PS-OCT measured only reflectivity and retardation of a sample, in recent years many proposals have been made to extract more information on the polarization properties of a sample. These improved techniques were used to measure and image Stokes vectors of the backscattered light,[7,28] Müller matrix [32] and Jones matrix [21] distribution in biologic samples.

While Müller and Jones matrices contain the maximum possible information on the polarizing properties of a sample, the images of Müller matrix and Jones matrix elements are difficult to interpret. Furthermore, the measurement of these matrices requires either several measurements with different input and analyzer polarization states [32] or the use of two light sources illuminating the sample with different input polarization states simultaneously,[21] which makes the measurement more time consuming or the instrument more complex. An important parameter of birefringence with straightforward physical interpretation is the slow birefringent axis of a sample. In fibrous tissues where birefringence is caused by form birefringence, this parameter is a measure of the fiber orientation. We have recently developed a PS-OCT method that measures and images three parameters: reflectivity, retardation, and (cumulative) slow axis orientation simultaneously with only a single A-scan per measurement location.[16]

Figure 1 shows a sketch of the instrument. The optical setup is based on the original polarization sensitive low coherence interferometer first described by Hee et al.[15] A super luminescent diode (SLD) emits a beam with center wavelength $\lambda_0 = 828$ nm and a bandwidth of $\Delta\lambda \approx 22.4$ nm, corresponding to a round trip coherence length of $\lambda_c \approx 13.5\ \mu$m. This beam illuminates, after being vertically polarized, a Michelson interferometer where it is split by a non-polarizing beam

splitter (NPBS) into a reference and a sample beam. The reference beam transmits quarter wave plate QWP2, oriented with its fast axis at 22.5° to the horizontal, and is reflected by a retroreflector and a reference mirror. After backpropagating through QWP2, the orientation of the beam polarization plane is at 45° to the horizontal, providing equal reference power in two orthogonal polarization states. The quarter wave plate QWP1 in the sample arm is oriented at 45° to provide circularly polarized light to the sample. After reflection at the sample and propagating back through QWP1, the light in the sample arm is in an elliptical polarization state containing information on the birefringence and optic axis orientation of the sample. After recombination with the reference beam at the interferometer beam splitter, both beam components are directed towards a polarization sensitive two-channel detection unit.

Three dimensional data sets are obtained by recording A-scans (z) on a two dimensional (x-y) lateral matrix on the sample. A-scans are recorded by shifting the retro reflector; a focusing lens mounted on the same translation table ensures dynamic focusing (matching of coherence gate and focal point in the sample).[29] Contrary to standard OCT and earlier versions of PS-OCT, not only the envelopes of the interferometric signals are recorded. Instead, for each detection channel an independent detector/amplifier/AD-converter combination records the whole interference signal $I_{H,\,V}(z)$ (H, V: horizontal and vertical polarization channel, respectively). The axial resolution is equal to the round trip coherence length l_c. In our case, the transversal resolution is determined by the step increments in transverse direction (100 μm). A 3D data set consists of 80 × 80 A-scans each of 2.5 mm length.

Calculation of polarization states

The polarization state of a fully polarized light beam traversing polarizing optical elements can be calculated by the Jones formalism.[19,22] The beam incident on the Michelson interferometer, after passing the polarizer, is in a linear, vertical polarization state. Its Jones vector can be written as:

$$\vec{E} = \begin{pmatrix} 0 \\ 1 \end{pmatrix} \qquad (1)$$

In this notation, we ignored a term oscillating with light frequency and set the electric field amplitude = 1. The upper and lower components of the vector in equation (1) correspond to the horizontal and vertical components of the electric field vector. The Jones vector of a beam traversing an optical element can be found by multiplying the Jones vector of the incident beam by the Jones matrix corresponding to the optical element. The Jones matrix is a 2 × 2 matrix consisting of - usually complex - elements. If more than one optical element is traversed, the input Jones vector has to be multiplied by the Jones matrices of each element, in the order they are transmitted by the beam.

The reference beam passes both, the beam splitter and the quarter wave plate QWP2, twice. The effect of the beam splitter is simply to reduce the intensity of the reference beam by a factor of 2 at every pass, leading to a total intensity reduction of a factor of 4, equivalent to a reduction in field amplitude by a factor of 2. The Jones matrix of a general retarder of retardation δ and fast axis orientation θ_f is:[13]

$$J(\delta,\theta_f) = \begin{bmatrix} \cos^2(\theta_f) + \sin^2(\theta_f)\cdot\exp(-i\delta) & \cos(\theta_f)\cdot\sin(\theta_f)\cdot(1-\exp(-i\delta)) \\ \cos(\theta_f)\cdot\sin(\theta_f)\cdot(1-\exp(-i\delta)) & \cos^2(\theta_f)\cdot\exp(-i\delta) + \sin^2(\theta_f) \end{bmatrix} \qquad (2)$$

For the reference beam, δ = 90° and θ_f = -22.5°. The Jones vector of the reference beam, after double passing QWP2 (and the beam splitter) is:

$$E_r = \frac{1}{2} J_{QWP2}\cdot J_{QWP2}\cdot\begin{pmatrix} 0 \\ 1 \end{pmatrix} = \frac{1}{2\sqrt{2}}\begin{pmatrix} 1 \\ 1 \end{pmatrix} \qquad (3)$$

This is a linearly polarized beam with its polarization axis oriented at 45°, providing equal reference intensity for both, the horizontal and the vertical polarization component, which are separated by the polarizing beam splitter PBS of the detection unit. Furthermore, no phase shift occurs between the two polarization components (this would cause at least one of the vector components to have an imaginary part). Therefore, the reference beam influences neither the intensity ratio nor the phase of the interference signals recorded in the two detection channels. The sample beam passes the beam splitter QWP1 and the sample (reflectivity: R) twice each. Again, the effect of the beam splitter is simply to reduce the field amplitude by a factor of 2. QWP1 has retardance and axis values of $\delta = 90°$ and $\theta_f = 45°$, respectively. The change of polarization state caused by the sample is described by J_{sample}, a general retardation matrix of the form given by equation (2). The Jones vector of the sample beam, after exiting the interferometer, is:

$$E_s = \frac{1}{2} J_{QWP1} \cdot J_{sample}(\delta, \theta_f) \cdot \sqrt{R} \cdot J_{sample}(\delta, \theta_f) \cdot J_{QWP1} \cdot \begin{pmatrix} 0 \\ 1 \end{pmatrix} = \frac{\sqrt{R}}{2} \begin{pmatrix} \cos(\delta)\exp(-i\delta) \\ \sin(\delta)\exp(i(\pi - \delta - 2\theta_f)) \end{pmatrix} \quad (4)$$

Determination of sample reflectivity, retardation, and axis orientation

As is well known from the theory of partial coherence interferometry, a sample interface located at depth position z_0, and with reflectivity R, gives rise to an intensity $I_k(z)$ recorded by the detector in channel k:[1]

$$I_k(z) = I_{r,k} + I_{s,k} + 2\sqrt{I_{r,k} I_{s,k}} \cdot |\gamma(z - z_0)| \cdot \cos(\Phi_k) \quad (5)$$

$I_{r,k}$ and $I_{s,k}$ are the intensities that would be recorded at the detector k from the reference mirror and the sample interface, respectively, without interference; k = H,V for the horizontal and vertical polarization state, respectively, $\Phi_k = 2\pi(z\text{-}z_0)/\lambda_0$ is the corresponding phase term of the oscillating interference signal, and $|\gamma(z\text{-}z_0)|$ is the modulus of the complex degree of coherence.

With equations (4) and (5), and with $I_{r,k} \propto E_{r,k}^2$ and $I_{s,k} \propto E_{s,k}^2$, ($E_{r,k}$ and $E_{s,k}$ are given by equations (3) and (4)), we can derive the physical parameters: reflectivity R, retardation δ, and fast optic axis orientation θ_f. To determine reflectivity and retardation, we need only the envelope of the AC term of equation (5). This is usually obtained by AC coupling the detector signal and subsequently rectifying and low pass filtering the amplified signal. However, to measure the optic axis orientation, we need the phase difference $\Delta\Phi = \Phi_V - \Phi_H$ occurring between the two signals. Therefore, we use a different approach. After AC coupling, the full interferometric signal is recorded. Amplitude $A_k(z)$ and phase $\Phi_k(z)$ of the oscillating term of each interference signal at any depth are extracted from the complex function:

$$\tilde{A}_k(z) = I_k(z) + i \cdot \mathbf{H}\{I_k(z)\} = A_k(z) \cdot \exp[i \cdot \Phi_k(z)] \quad (6)$$

which is determined by analytic continuation of the measured interference signal $I_k(z)$ by use of the Hilbert transform **H**.

Comparing equations (5) and (6), we see that $A_k(z) = 2\sqrt{I_{r,k} I_{s,k}} \cdot |\gamma(z - z_0)|$. From equation (4), we can now see that maps of sample reflectivity R and phase retardation δ can be obtained by:[15]

$$R(z) \sim A_H(z)^2 + A_V(z)^2 \quad (7)$$

$$\delta(z) = \arctan\left(\frac{A_V(z)}{A_H(z)}\right) \quad (8)$$

Furthermore, equation (4) indicates that only the signal corresponding to the vertical polarization state (channel V) depends on the sample fast axis orientation θ_f, while both signals oscillate

synchronously with retardation δ. Therefore, the axis orientation is directly encoded in the phase difference $\Delta\Phi(z) = \Phi_V(z) - \Phi_H(z)$ which can be obtained with the help of equation (6):

$$\theta_f(z) = (180° - \Delta\Phi(z))/2 \quad (9)$$

The slow axis orientation is oriented perpendicular to the fast axis:

$$\theta_s = -(\Delta\Phi(z))/2 \quad (10)$$

On OCT tomograms, backscattered signal intensity ($\sim\sqrt{R}$) is displayed on a logarithmic false color scale, δ and θ_s are displayed on linear false color scales. The unambiguous ranges of δ and θ_s determination are 0° to 90° and 0° to 180°, respectively.

It should be pointed out that the interpretation of the slow axis data requires some care: (i) the algorithm used to calculate θ_s causes a 90° change in θ_s at depth positions z where δ crosses 90° (or multiples of 90°). (ii) If several layers with different slow axes are stacked on top of each other, the measured value θ_s (z), at a given depth position z, is a cumulative, or effective, axis: it is the slow axis of a single layered birefringent plate that would, on double pass, give rise to the same change of polarization state as the multi-layered sample does up to a depth z. To differentiate the axis orientations of individual layers would require that (a) these individual layers are resolved, i.e. are thicker than the coherence length, and (b) to use an algorithm based on the information obtained on the overlying layers and propagating the polarization state from layer to layer.

Sample preparation

Human donor corneas were received from the eye bank (Department of Ophthalmology, General Hospital, Medical University of Vienna). Only corneas that were not hepatitis B negative and therefore could not be used for transplantation were used in this study. Full-thickness corneal transplants were stored in Optisol (Chiron, CA) and imaged by PS-OCT within two weeks after enucleation. The corneas had been extracted with a small scleral ring still attached which ensured sufficient stability during handling and measurement. For PS-OCT imaging, the corneas were mounted in a specimen holder consisting of a metal case sealed with a glass window through which imaging was performed. The metal case was filled with Optisol to prevent dehydration during the imaging.

RESULTS

We measured three dimensional datasets of in vitro human corneas. 80 × 80 A-scans in x and y direction, with a depth range of 2.5 mm, were recorded. The step width in both directions was 100 μm (i.e. a transversal area of 8 mm × 8 mm is covered). The depth resolution is 13.5 μm. Figure 2 shows horizontal cross sectional images (x-z) derived from the three dimensional dataset through the center (apex) of the cornea. Figure 2 A shows an intensity image (logarithmic color scale). Figure 2 B shows a retardation image (linear color scale). The parts of the image shown in gray correspond to regions where the signal intensity is not significantly above the noise level (in this case, a reliable calculation of retardation and axis values is not possible). The retardation increases in radial direction. Towards the periphery, the retardation increases with depth. At the margin of the image of figure 2 B, ~ 4 mm from the corneal apex, the color indicating retardation makes ~ one full oscillation from blue at the anterior corneal surface over red to blue again at the posterior surface, indicating a retardation of ~ 180° over the full corneal thickness at the periphery. Figure 2 C shows the slow axis distribution across the cornea (linear color scale). The cumulative slow axis varies in radial direction, however, is roughly constant over the corneal thickness at a given transversal position (except for the 90° color change caused by the algorithm at positions where $\delta > 90°$).

Figure 3 shows en face PS-OCT images derived from the same 3D data set of the same cornea. Retardation (Fig. 3 A) and slow axis orientation (Fig. 3 B) distribution corresponding to the back surface of the cornea are shown (the posterior surface was approximated by a polynomial fit to

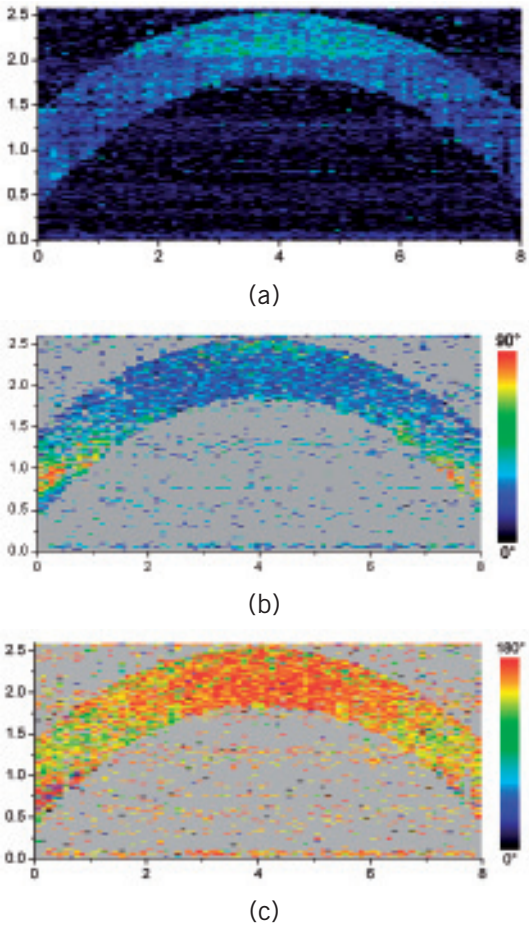

Fig. 2. Horizontal cross sectional PS-OCT images of human cornea in vitro. Axis labels: (optical) distances [mm]. (a) Reflectivity image (logarithmic color scale); (b) retardation image (linear color scale); (c) slow axis orientation image (linear color scale). Adapted from Götzinger et al.[14] by permission from the SPIE.

the interface as measured from the OCT reflectivity data set). Figure 3 A shows that the retardation is lowest in the center and increases in radial direction. Figure 3 B indicates that the slow axis orientation varies approximately linearly with azimuth angle. Along the positive y-axis, $\theta_s \approx 0°$; θ_s increases in clockwise direction, to ~ 90° along the positive x-axis, and further to ~ +180° near the negative y-axis. Due to the π ambiguity of the used algorithm, the axis orientation can only be mapped from 0° to 180°. Because of the above mentioned 90° color jumps in θ_s at positions where $\delta > 90°$, the overall image pattern of approximately constant θ_s at a given azimuth angle is disturbed at the periphery. For a better, undisturbed view of the slow axis orientation pattern, we derived an additional *en face* image of slow axis orientation that corresponds to a position in the middle of the cornea, ~ half way between anterior and posterior corneal surface. This image is shown in figure 3 C. Since $\delta < 90°$ in this depth throughout the cornea, the axis distribution pattern is undisturbed. A comparison of figures 3 B and C further indicates that the axis orientation is roughly constant in depth.

PS-OCT data sets were recorded in a similar way in five donor corneas. The results were essentially similar to those observed in figures 2 and 3. Central corneal retardation (at the posterior surface) ranged from 13° to 30°. Although slow axis orientations within the total interval 0° to

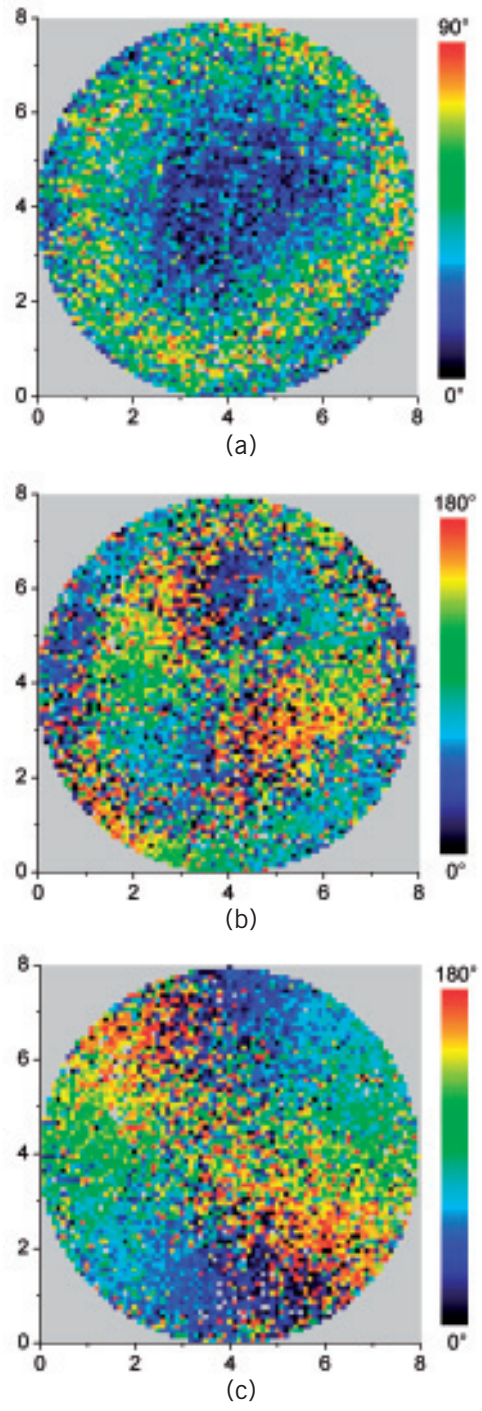

Fig. 3. En face PS-OCT images of human cornea in vitro. Axis labels: distances [mm]. (a) Retardation distribution at posterior corneal surface (linear color scale); (b) cumulative slow axis distribution at posterior corneal surface (linear color scale); (c) cumulative slow axis distribution approximately half way between anterior and posterior corneal surfaces (linear color scale). Adapted from Götzinger et al.[14] by permission from the SPIE.

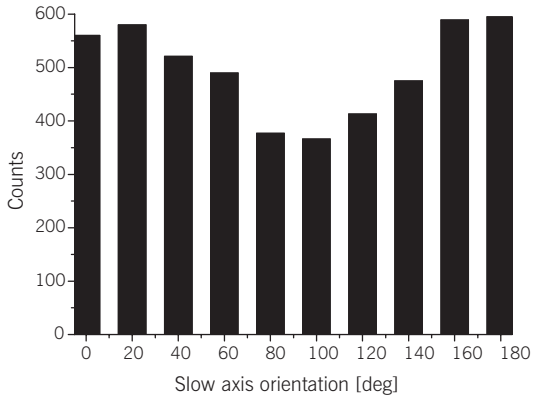

Fig. 4. Histogram of slow axis distribution in human cornea in vitro.

180° are observed, they are not evenly distributed. Figure 4 shows a histogram of slow axis distribution of one of the five corneas which clearly illustrates this feature. There is a frequency maximum for axis values near 0° and 180°, and a minimum for values near 90°. It should be mentioned that figure 4 just indicates that there is an overall preferential orientation of slow axis within the cornea; since the excised corneas were not marked, the absolute orientation of the axis with respect to the horizontal meridian of the intact eye is not available.

Further experiments with a cornea tilted about the horizontal axis (not shown here), revealed that the retardation is always lowest at perpendicular sample beam incidence, which does not coincide with the apex in the case of the tilted cornea.[14] Similarly, the point of rotation, about which the slow axis increases with azimuth angle, is also shifted from the apex to the point where the sample beam incidence is perpendicular to the corneal surface. These results clearly demonstrate that the corneal apex is not a center of symmetry with respect to corneal birefringence; rather, the observed birefringence effects are caused by the angle of incidence that the sample beam makes with the corneal surface.

Preliminary experiments

Since the completion of the in vitro measurements on healthy normal corneas, further preliminary experiments were carried out on diseased donor corneas in vitro and on healthy corneas in vivo.

Figure 5 shows results derived from a 3D data set obtained from a keratoconus cornea explanted during a penetrating keratoplasty at the Department of Ophthalmology, General Hospital, Medical University of Vienna. The data sets were recorded in a similar way as described above, the main difference was that the diameter of the explanted cornea was slightly smaller (6 mm) and the specimen holder was modified accordingly. Figures 5 A and B show *en face* tomograms of retardation and slow axis orientation, respectively, derived at the posterior corneal surface. Figures 5 C and D show corresponding horizontal (x-z) cross sections derived along the horizontal red line shown in figures 5 A and B; figures 5 E and F show corresponding vertical cross sections (y-z, derived along the vertical red lines in figures 5 A and B). Compared to the PS-OCT images obtained in the normal corneas (figures 2 and 3), both, the retardation and axis orientation patterns of the keratoconus cornea are heavily distorted. Similar distortions can be observed in corneal scars.

Figure 6 shows PS-OCT cross sectional images (x-z) obtained with a modified instrument in a human cornea in vivo. The modified instrument was designed for high-speed imaging and is based on a transversal scanning scheme that generates the carrier frequency by acousto optic frequency shifting.[17] Details of the setup will be reported elsewhere.[26] There is an interesting diffe-

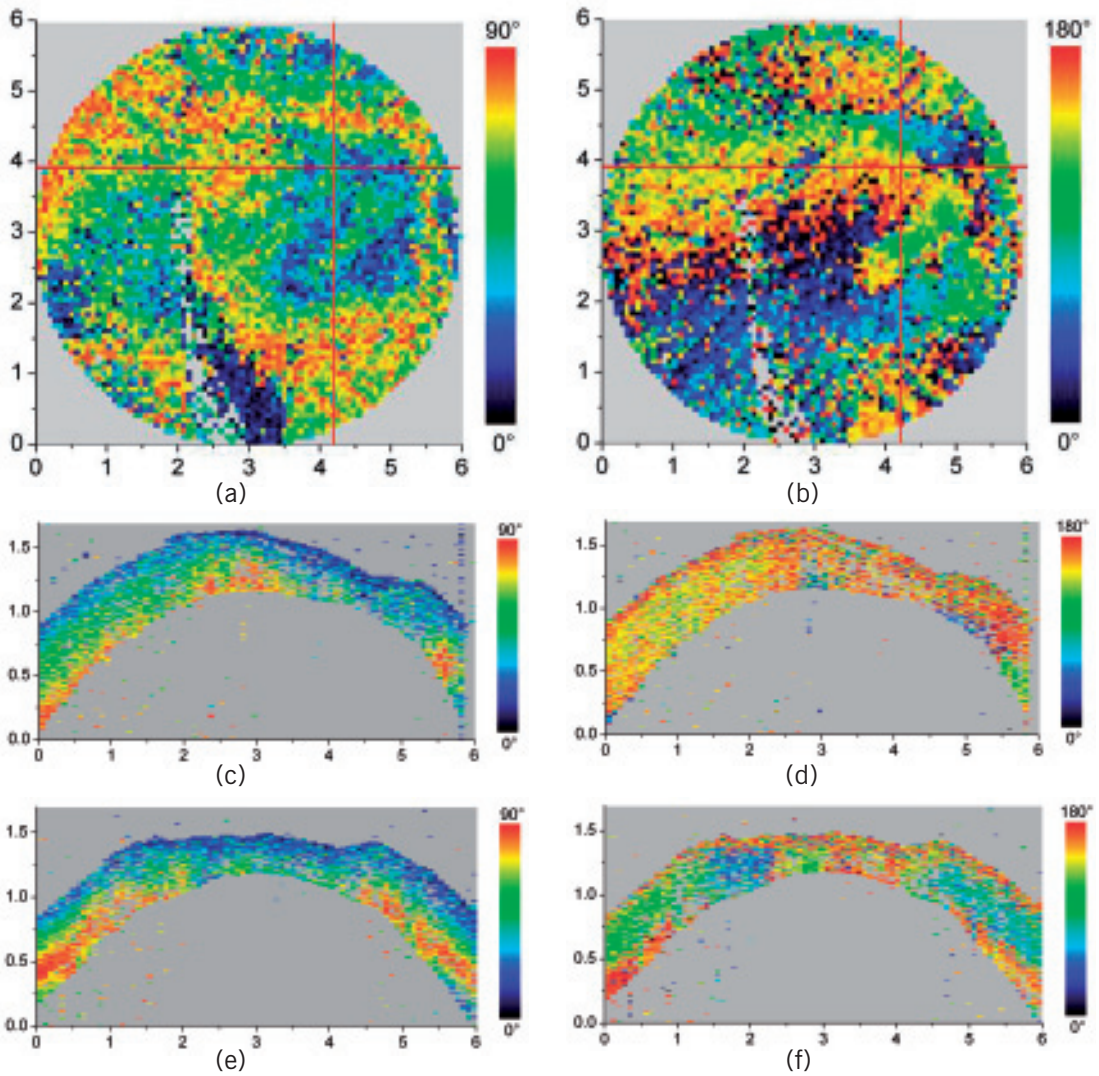

Fig. 5. 3D PS-OCT data set of keratoconus cornea in vitro. En face images of retardation distribution (a) and cumulative slow axis distribution (b); the red lines indicate the positions of the cross sectional images (c - f). (c) and (d) horizontal cross sectional images of retardation and slow axis distribution, respectively; (e) and (f) vertical cross sectional images of retardation and slow axis distribution, respectively.

rence near the center of the retardation image (Fig. 6 B), as compared to that of the in vitro images. Light scattered back roughly perpendicular to the corneal surface (from beneath the apex) is depolarized. This is indicated by the greenish color in the retardation image. The color in the retardation image might be confused with a retardation near 45°, however, the color is caused merely by a mix of random retardation values. It should be pointed out that this depolarization takes only place in the directly backscattered light. The transmitted light still has a high degree of polarization corresponding to low retardation, which can be observed from light backscattered at deeper structures (anterior lens surface, iris) not shown here. A similar effect of depolarization of directly backscattered light while maintaining the polarization of transmitted light has recently been reported for the stratum corneum of human skin.[27] Such an effect could be caused by

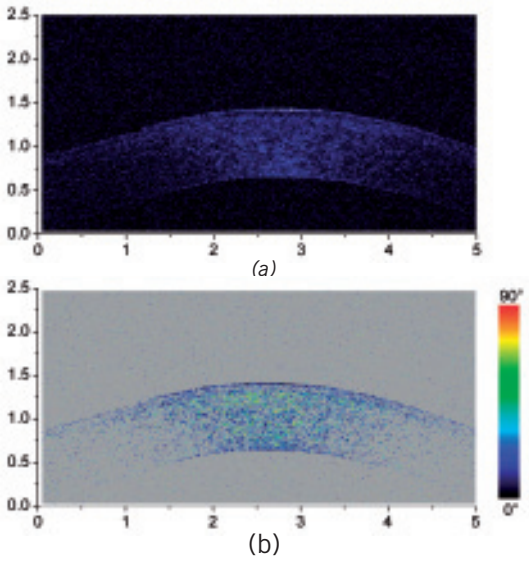

Fig. 6. Horizontal cross sectional PS-OCT images of human cornea in vivo. Axis labels: (optical) distances [mm]. (a) Reflectivity image (logarithmic color scale); (b) retardation image (linear color scale).

scattering at large, non-spherical particles, however, the details of the origin of the depolarized backscattered light are not yet clear and require further studies.

DISCUSSION

The results of our measurements on the birefringence of the normal human cornea in vitro by PS-OCT can be summarized as follows: corneal retardation is low for beams incident approximately perpendicular to the corneal surface. At oblique angles, measured birefringence increases with deviation from perpendicular incidence. In case of illumination of the cornea with beams parallel to the vision axis, as used in the experiments corresponding to figures 2 to 4, this yields a circular symmetric retardation pattern where retardation is lowest near the apex and increases towards the periphery. The cumulative slow axis orientation at a given lateral position is roughly constant with depth. With the illumination scheme parallel to the vision axis, the slow optic axis is not constant across the cornea but oriented approximately tangentially along circles that are centered at the apex. In terms of inclination of the corneal surface, the slow axis is perpendicular to a plane made up by the incident beam and a vector perpendicular to the corneal surface. A slight preferential slow axis orientation is overlayed over this general pattern.
These results can be explained by a birefringence model based on a stack of thin birefringent lamellae with two preferential, nearly orthogonal, fibril orientations, superimposed on a background of lamellae with random orientation.[6,25] To explain our results we use the sketch provided in figure 7. Figure 7 shows a section along the horizontal meridian through a thin stromal layer composed of two lamellae with orthogonal fibril orientation, stacked on top of each other (the full thickness stroma consists of ~ 200 such lamellae). Two incident beam positions are indicated. If the beam illuminates the cornea at the apex (A), it transmits both lamellae perpendicular to their fibrils. The first lamella has its slow axis orthogonal to the drawing plane, the second one parallel to that plane. The opposite birefringence effects cancel each other, and net retardation is zero. Beam B illuminates the cornea at the periphery. The beam is still perpendicular to the fibrils of the first lamella, but not to those of the second one, which have, due to the corneal curvature, a component parallel to the incident beam. Since only those fibril compo-

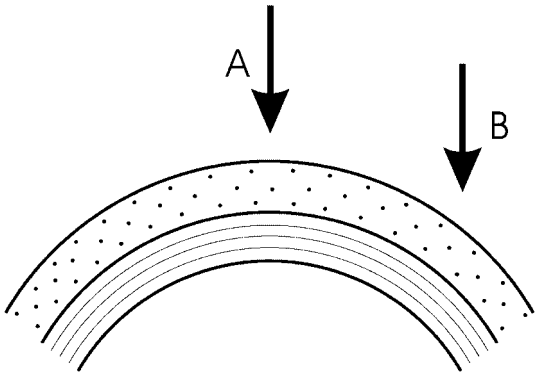

Fig. 7. Sketch of two stromal lamellae with fibril orientation perpendicular (upper layer) and parallel (lower layer) to the drawing plane. See text. Reproduced from Götzinger et al.[14] by permission from the SPIE.

nents that are oriented perpendicular to the incident beam contribute to the birefringence encountered by the beam, the cancellation of birefringence effects of the two layers will be incomplete at the periphery and a net birefringence will be observed. At increasing distance from the center, the fibrils in the second layer bend more towards the direction of the incident beam, therefore their vectorial component perpendicular to the beam decreases and the net birefringence observed increases with distance from the center. The observed net slow axis orientation will be parallel to the fibrils of the first layer (its birefringence dominates off the center, as mentioned above), i.e. orthogonal to the plane made up by the incident beam and the corneal surface vector, in agreement with our observations.

The corneal stroma consists of ~ 200 lamellae, ~ 2/3 of which are oriented similarly to those shown in figure 7. The remaining third is roughly randomly oriented, so the whole corneal stroma should have a birefringence behavior essentially similar to that discussed above. A slight prevalence of one lamella orientation gives rise to a net retardation and axis orientation even in the center of the cornea.[23,33] Since the stromal lamellae have a thickness of ~ 2 μm, and the coherence length of our SLD is ~ 10 μm (in the tissue), the individual lamellae cannot be resolved, and only a cumulative net birefringence is observed.

The birefringence model was so far explained for a horizontal section across the center of the cornea, where we took advantage of the fact that the fibrils in the corneal lamellae have preferential orientations in horizontal and vertical directions. However, the model should be generally valid which can be seen by considering that a fibril of any orientation can be vectorially decomposed in tangential and radial components. While the tangential components will always be perpendicular to the incident beam, the radial components will bend more and more towards the direction of the incident beam as the corneal periphery is approached.

If we compare our results to published data on human corneal birefringence, we find similarities but also deviations. The majority of studies performed so far measured retardation and axis orientation only at single points, typically near the center of the cornea. A recent comprehensive study performed in both eyes of 73 normal subjects reported a wide variation of retardance, ranging from 0 to 95 nm (single pass) at a wavelength of 585 nm, the mean value was approximately 50 nm.[23] Our central retardance values range from 13° to 30° or 30 to 69 nm (at a wavelength of 828 nm) and are therefore well within the reported range. The slow optic axis is reported to have a preferential orientation of typically 20° nasally downward, but also with large inter-individual variability.[23] Our results indicate that the slow axis orientation varies across the corneal surface. A comparison with a measurement at a single point is difficult. However, if averaged over a larger area, we find that there is a prevalence of one slow axis orientation which might be called a net slow axis of the cornea. Since the excised corneas were not marked, we do not know the absolute orientation of the net slow axis.

Some of the previously reported studies also measured retardation as a function of lateral position across the cornea.[4-5,31] Van Blockland and Verhelst [31] report a retardation distribution of saddleback shape, i.e. an increase of retardation from the center towards the periphery along a vertically oriented meridian, while retardation decreases towards the periphery along the horizontal meridian. This is in contradiction to our results and those reported by Bour and Lopez Cardozo [4] and Bueno and Vargas-Martin [5] who also found an increase of retardation towards the periphery, independent of the meridian orientation. The discrepancy might be explained by the fact that Van Blockland and Verhelst used light reflected at the retina for their measurements, which might has changed the polarization state. Two previous studies measured optic axis distribution across the cornea.[5,20] Bueno and Vargas-Martin [5] used a liquid-crystal imaging polariscope to measure birefringence in human corneas in vivo. They illuminated the eye with a collimated light beam and used light reflected at the iris to measure the distribution of retardation and axis orientation in the cornea. Because the iris reflection was used, the central part of the cornea could not be measured. They found that the axis was approximately constant across the cornea. The latter result is in contradiction to our findings. Jaronski and Kasprzak [20] used a phase stepping imaging polarimeter to measure birefringence in a human cornea in vitro. In figure 5 A of their paper, a non-uniform axis distribution with an axis orientation increasing with azimuth angle in large parts of the cornea can be observed. Although the situation is not so clear in the center of the cornea, and the authors do not further comment or interpret this image, we think there is a general agreement with our results.

To clarify the contradictory results we repeated the experiment of Bueno and Vargas-Martin [5] with a simplified setup in an in vitro cornea.[14] The result was in good qualitative agreement with a varying optic axis oriented in a tangential pattern around the apex. This is in agreement with our PS-OCT results and that of Jaronski and Kasprzak.[20] The deviation to the results reported in Bueno and Vargas-Martin[5] is not easy to explain. Reasons might be increased speckle noise by using the reflection at the rough iris surface in Bueno and Vargas-Martin [5] and the use of a complicated equation sensitive to divisions by zero. On the other hand, the iris itself has an ordered structure which has some circular symmetry. This structure might change the polarization state of the backscattered beam in a way that makes it unreliable for subsequent corneal birefringence determination.

The results of our study might have some implications for the use of ophthalmic diagnostic instruments operating with polarized light. Especially scanning laser polarimetry (SLP) of the retinal nerve fiber layer requires that the corneal birefringence is compensated for. The first generation of these instruments assumed a fixed corneal retardation for the entire population. Since this assumption is not true,[23] the newest generation of SLP instruments has a variable corneal compensator capable of compensating each cornea individually. This can improve the reliability of the SLP as a glaucoma detection device considerably.[33] Our results indicate that even within a single cornea, the optic axis orientation varies. However, the geometry of the light path of the SLP is different from that used in our study. A SLP illuminates the eye not parallel to the vision axis but with a tilting beam that has its pivot point near the nodal point of the eye. In this case the incident beam remains close to a perpendicular orientation to the corneal surface over the transversal scanning range. Therefore, we assume that the sampling beam of the SLP encounters essentially the net retardance and optic axis orientation that we measured near the center of the cornea. However, the beam diameter should not be too large, otherwise different parts of the scanning beam (across the diameter) would encounter different corneal birefringence and the compensation might be incomplete.

In case of corneal pathologies, such as keratoconus, the situation seems to be completely different. X ray diffraction studies have shown that fibril orientation patterns change considerably in this disease.[6] Preliminary PS-OCT experiments carried out in keratoconus (Fig. 5) and in corneal scar tissue indicate that the birefringence patterns observed in figures 2 to 4 are dramatically changed. This might be used to study and diagnose corneal pathologies by PS-OCT. On the

other hand, these preliminary results indicate that techniques like SLP have to be used with caution in patients that suffer from corneal pathologies like keratoconus.

ACKNOWLEDGMENTS

The authors thank Prof. C. Skorpik (Department of Ophthalmology, Medical University of Vienna) for providing corneal explants, and Mr. H. Sattmann and Mr. L. Schachinger for technical assistance. Financial assistance from the Austrian Fonds zur Förderung der wissenschaftlichen Forschung (FWF grants P14103-MED and P16776-N02) is acknowledged.

REFERENCES

(1) BORN M., WOLF E. – Principles of Optics (chapter 10). Pergamon, Oxford 1987; 505-508
(2) BOUMA B.E., TEARNEY G.J. – Handbook of optical coherence tomography. Marcel Dekker, New York 2002
(3) BOUR L.J. – Polarized light and the eye. In: Charman W.N. (ed.) Visual optics and instrumentation. CRC Press, Boca Raton, FL 1991; 310-325
(4) BOUR L.J., LOPEZ CARDOZO N.J. – On the birefringence of the living human eye. Vision Res 1981; 21: 1413-1421
(5) BUENO J.M., VARGAS-MARTIN F. – Measurements of the corneal birefringence with a liquid-crystal imaging polariscope. Appl Opt 2002; 41: 116-124
(6) DAXER A., FRATZL P. – Collagen fibril orientation in the human corneal stroma and its implication in keratoconus. Invest Ophthalmol Vis Sci 1997; 38: 121-129
(7) DE BOER J.F., MILNER T.E., NELSON J.S. – Determination of the depth resolved Stokes parameters of light backscattered from turbid media using polarization sensitive optical coherence tomography. Opt Lett 1999; 24: 300-302
(8) DE BOER J.F., MILNER T.E., VAN GEMERT M.J.C., NELSON J.S. – Two-dimensional birefringence imaging in biological tissue by polarization-sensitive optical coherence tomography. Opt Lett 1997; 22: 934-936
(9) DONOHUE D.J., STOYANOV B.J., MC CALLY R.L., FARRELL R.A. – Numerical modeling of the cornea's lamellar structure and birefringence properties. J Opt Soc Am A 1995; 12: 1425-1438
(10) DREHER A.W., REITER K., WEINREB R.N. – Spatially resolved birefringence of the retinal nerve fiber layer assessed with a retinal laser ellipsometer. Appl Opt 1992; 31: 3730-3749
(11) DUCROS M.G., DE BOER J.F., HUANG H.E., CHAO L.C., CHEN Z., NELSON J.S., MILNER T.E., RYLANDER H.G. III – Polarization sensitive optical coherence tomography of the rabbit eye. IEEE J Sel Top Quantum Electron 1999; 5: 1159-1167
(12) FERCHER A.F., HITZENBERGER C.K. – Optical Coherence Tomography. Progr Opt 2002; 44: 215-302
(13) GERRARD A., BURCH J.M. – Introduction to matrix methods in optics. John Wiley & Sons, London 1975; 212
(14) GÖTZINGER E., PIRCHER M., STICKER M., FERCHER A.F., HITZENBERGER C.K. – Measurement and imaging of birefringent properties of the human cornea with phase-resolved, polarization-sensitive optical coherence tomography. J Biomed Opt 2004; 9: 94-102
(15) HEE M.R., HUANG D., SWANSON E.A., FUJIMOTO J.G. – Polarization sensitive low coherence reflectometer for birefringence characterization and ranging. J Opt Soc Am B 1992; 9: 903-908
(16) HITZENBERGER C.K., GÖTZINGER E., STICKER M., PIRCHER M., FERCHER A.F. – Measurment and imaging of birefringence and optic axis orientation by phase resolved polarization sensitive optical coherence tomography. Opt Express 2001; 9: 780-790
(17) HITZENBERGER C.K., TROST P., LO P.W., ZHOU Q. – Three-dimensional imaging of the human retina by high-speed optical coherence tomography. Opt Express 2003; 11: 2753-2761
(18) HUANG D., SWANSON E.A., LIN C.P., SCHUMAN J.S., STINSON W.G., CHANG W., HEE M.R., FLOTTE T., GREGORY K., PULIAFITO C.A., FUJIMOTO J.G. – Optical coherence tomography. Science 1991; 254: 1178-1181
(19) HURWITZ H., JONES C.R. – A new calculus for the treatment of optical systems. II. Proof of the three general equivalence theorems. J Opt Soc Am 1941; 31: 493-499

(20) JARONSKI J.W., KASPRZAK H.T. – Generalized algorithm for photoelastic measurements based on phase stepping imaging polarimetry. Appl Opt 1999; 38: 7018-7025
(21) JIAO S., WANG L.V. – Jones-matrix imaging of biological tissues with quadruple-channel optical coherence tomography. J Biomed Opt 2002; 7: 350-358
(22) JONES C.R. – A new calculus for the treatment of optical systems. I. Description and discussion of the calculus. J Opt Soc Am 1941; 31: 488-493
(23) KNIGHTON R.W., HUANG X.R. – Linear birefringence of the central human cornea. Invest Ophthalmol Vis Sci 2002; 43: 82-86
(24) MAURICE D.M. – The structure and transparency of the corneal stroma. J Physiol (London) 1957; 136: 263-285
(25) NEWTON R.H., MEEK K.M. – The integration of the corneal limbal fibrils in the human eye. Biophys J 1998; 75: 2508-2512
(26) PIRCHER M., GOETZINGER E., LEITGEB R., FINDL O., HITZENBERGER C.K. – Imaging of polarization properties of human retina in vivo with phase resolved transversal PS-OCT. Opt Express 2004; 12: 5940-5951
(27) PIRCHER M., GOETZINGER E., LEITGEB R., HITZENBERGER C.K. – Three dimensional polarization sensitive OCT of human skin in vivo. Opt Express 2004; 12: 3236-3244
(28) SAXER C.E., DE BOER J.F., PARK B.H., ZHAO Y., CHEN C., NELSON J.S. – High speed fiber based polarization-sensitive optical coherence tomography of in vivo human skin. Opt Lett 2000; 25: 1355-1357
(29) SCHMITT J.M., LEE S.L., YUNG K.M. – An optical coherence microscope with enhanced resolving power in thick tissue. Opt Commun 1997; 142: 203-207
(30) STANWORTH A., NAYLOR E.J. – The polarization optics of the isolated cornea. Br J Ophthalmol 1950; 34: 201-211
(31) VAN BLOKLAND G.J., VERHELST S.C. – Corneal polarization in the living human eye explained with a biaxial model. J Opt Soc Am A 1987; 4: 82-90
(32) YAO G., WANG L.V. – Two-dimensional depth-resolved Mueller matrix characterization of biological tissue by optical coherence tomography. Opt Lett 1999; 24: 537-539
(33) ZHOU Q., WEINREB R.N. – Individualized compensation of anterior segment birefringence during scanning laser polarimetry. Invest Ophthalmol Vis Sci 2002; 43: 2221-2228

.....

Corresponding address:

Christoph K. Hitzenberger, PhD
Center for Biomedical Engineering and Physics
Medical University of Vienna
Währinger Str. 13
A-1090 Vienna, Austria
E-mail: christoph.hitzenberger@meduniwien.ac.at